Microstructure Evolution and Tensile Properties of Cold-Rolled and Annealed Fe-30Mn-0.14C-7Cr-0.26Ni Steel

XIAOMAN CHEN, JIAXIN ZHANG, JIANCHAO XIONG, YUHUI WANG, YUBIN ZHANG, TIANSHENG WANG, and YAN PENG

The carbide precipitation, microstructure evolution, and tensile properties of Fe-30Mn-0.14C-7Cr-0.26Ni (in wt pct) steel after cold rolling to 95 pct reduction followed by annealing at temperatures ranging from 600 °C to 900 °C for 1 hour were investigated. The results show that, when the annealing temperature is increased from 600 °C to 900 °C, the grain size increases from 0.65 ± 0.30 to 5.75 ± 3.87 μm. When the annealing temperature is 600 °C, $Cr_{23}C_6$ carbides begin to precipitate. When the annealing temperature is increased from 600 °C to 800 °C, the average size of carbides increases from 39 to 69 nm. When the annealing temperature is increased to 900 °C, no carbides are produced due to the increased solubility of C in the austenite matrix. Ultrafine grains (~ 0.8 ± 0.58 μm) with a large amount of nanoscale carbides (~ 53 ± 21.8 nm) were obtained after annealing at 700 °C, resulting in a good combination of yield strength (679 MPa) and total elongation (38.4 pct). The fraction of deformation twins within the samples under different tensile strains was calculated, and it was revealed that grain refinement can seriously inhibit the generation of deformation twins. In addition, it has been found that grain refinement strengthening, precipitation strengthening, and dislocation strengthening have significant effects on yield strength, while the effects of solution strengthening and lattice friction are relatively weaker.

https://doi.org/10.1007/s11661-021-06345-y

I. INTRODUCTION

HIGH-MANGANESE twinning-induced plasticity (TWIP) steel is one of the most highly potential materials in the automobile industry.[1–3] The available research on Fe-Mn-C steels with high manganese content concerns the microstructure evolution in the deformation process,[4–8] such as deformation twins,[9–11] ε-martensite,[12,13] and the stacking fault.[14–16] A low stacking-fault energy is a necessary condition to activate the generation of deformation twins in the deformation process; however, it is not enough.[3] Bouaziz *et al.*[3] reported that the deformation mechanism of Fe-30Mn is the occurrence of dislocation slip, while Allain *et al.*[17] indicated that the deformation mechanism of Fe-22Mn-0.6C, Fe-17Mn-0.9C, and Fe-12Mn-1.2C (all in wt pct) is a combination occurrence of dislocation slip and deformation twinning. Therefore, the Mn and C elements may be a key factor for the activation of deformation twinning.[3] In addition, the generation of deformation twins under tensile deformation is closely related to the grain size, dislocation density, and crystal orientation of the material.[18,19] Koyama *et al.*,[20] Gutierrez-Urrutia *et al.*,[21] and Kang *et al.*[22] reported that the presence of fine grains inhibits the formation of twins and the twin stress increases with decreasing grain size. Further, deformation twins can improve not only the elongation but also the tensile strength of TWIP steels.[23]

The precipitation of carbides is important to obtain materials with an efficient combination of strength and ductility, which has been reported for complex alloys. The strength and plasticity of complex alloys can be improved by introducing nanoscale precipitations.[24] Zhang *et al.*[25] reported the presence of Cr-rich $M_{23}C_6$-type carbides in the $Al_{0.3}Cu_{0.5}CrFeNi_2$ high-entropy alloy. The formation of $Cr_{23}C_6$ improves the

XIAOMAN CHEN, YUHUI WANG, and TIANSHENG WANG are with the National Engineering Research Center for Equipment and Technology of Cold Strip Rolling, Yanshan University, Qinhuangdao 066004, China and also with the State Key Laboratory of Metastable Materials Science and Technology, Yanshan University, Qinhuangdao 066004, China. Contact e-mail: yhwang@ysu.edu.cn JIAXIN ZHANG, JIANCHAO XIONG, and YAN PENG are with the National Engineering Research Center for Equipment and Technology of Cold Strip Rolling, Yanshan University. Contact e-mail: jxzhang@ysu.edu.cn YUBIN ZHANG is with the Department of Mechanical Engineering, Technical University of Denmark, DK-2800 Kgs, Lyngby, Denmark.

Manuscript submitted February 20, 2021; accepted May 30, 2021.
Article published online July 1, 2021

strength of the material without loss of elongation. The Cr-rich $M_{23}C_6$-type carbides have hardly been systematically investigated in Fe-Mn-C high-manganese steels, while the research on stainless steel has mainly focused on its microstructure evolution during heat treatment. Nevertheless, in recent years, the precipitation of V, Nb, and Ti has been investigated in Fe-Mn-based shape memory alloys and high-manganese steels.[3,26–30] For example, Scott *et al.*[26] added Ti, Nb, and V to a Fe-Mn-C high-manganese steel and found that TiC, NbC, and VC precipitates were formed in the structure of the cold-rolled strip. In addition, the grains were refined due to the formation of carbides. Due to the combined effect of these two aspects, steels with added Ti, Nb, and V can have a higher yield strength compared to those with no addition of Ti, Nb, and V.

Similarly, Cr is another strong element, which can be easily combined with C to form carbides in alloys. Therefore, in this article, 7 wt pct Cr was added to the investigated steel, which induced grain refinement strengthening, solid solution strengthening, and precipitation strengthening, improving its yield strength. Cr is known to significantly improve the corrosion resistance of Fe-based alloys,[31,32] since the addition of Cr can improve their passivation ability. The improved corrosion resistance can overcome the limitations that prevent the application of such alloys in certain environments. Moreover, the addition of Ni can improve the toughness of the alloy and reduce its ductile brittle transition temperature, thus improving its mechanical properties at low temperature.[33,34]

In this study, a Fe-30Mn-0.14C-7Cr-0.26Ni (in wt pct) steel with different grain sizes was successfully prepared by traditional cold rolling and subsequent annealing at different temperatures. The microstructure of the obtained materials was characterized by scanning electron microscopy (SEM) and transmission electron microscopy (TEM). The test steel exhibited good mechanical properties due to the generation of deformation twins in combination with the various strengthening mechanisms. In addition, the contribution of various strengthening methods to yield strength was determined through a mathematical model. The results revealed that fine-grain strengthening, precipitation strengthening, and dislocation strengthening have significant effects on yield strength, while the effects of solution strengthening and lattice friction are relatively weak.

II. MATERIALS AND METHODS

Table I shows the chemical composition of the steel used in this study. The investigated steel with a main chemical composition of Fe-30Mn-0.14C-7Cr-0.26Ni (in wt pct) was melted by vacuum induction. In a traditional Fe-Mn-C ternary alloy, 7 wt pct Cr and 0.26 wt pct Ni were added. The addition of 7 wt pct Cr cannot only induce the generation of carbides, but also ensure the presence of Cr in the matrix, resulting in solution strengthening and inhibition of austenite intergranular corrosion. The addition of 0.26 wt pct Ni can improve the matrix toughness and the low-temperature mechanical properties of the test steel. Due to the high Mn content, there is no need to add more Ni to stabilize the austenite, and as a result, the cost is reduced as well. The ingots were heated to 1200 °C and held for 4 hours, and then forged at 900 °C to produce a 22-mm-thick and 40-mm-wide plate. Subsequently, the hot-forged plate was heated at 1100 °C for 1 hour and then was cold rolled up to a thickness reduction of 95 pct. This was followed by annealing at 600 °C, 700 °C, 800 °C, and 900 °C for 1 hour to obtain a laminated composite structure composed of recovered and recrystallized layers and fully recrystallized grains. The structure of the cold-rolled plate was a fully austenitic structure, which has also been reported in the literature.[34] Samples with different microstructure were obtained by 95 pct cold rolling followed by annealing at 600 °C to 900 °C for 1 hour.

Uniaxial tensile tests with the tensile direction aligned along the rolling direction (RD) were performed using an MTS tensile testing machine at an initial strain rate of 10^{-3} s^{-1} at room temperature. Tensile specimens with a gage length of 13 mm, width of 5.2 mm, and thickness of 1 mm were prepared from the annealed sample. Three tensile tests were performed at each annealing temperature.

The microstructure of the cold-rolled samples annealed at 600 °C to 900 °C for 1 hour and that of the samples subjected to different strains after annealing at 600 °C to 900 °C for 1 hour were analyzed by SEM (FEI Scios scanning electron microscope; $V = 5$ kV and $I = 0.4$ nA), TEM (FEI Talos 200X transmission electron microscope; $V = 200$ kV), and electron backscatter diffraction (EBSD; EDAX EBSD; $V = 20$ kV and $I = 6.4$ nA). X-ray diffraction (XRD) analysis of the samples annealed at 600 °C to 900 °C for 1 hour was conducted using a D/max 2400 diffractometer equipped with Cu K_α radiation. The scan rate was 0.02 deg s^{-1}, the 2-theta range was 40 to 100 deg, the working voltage was 40 kV, and the working current was 200 mA. For the SEM observations, the surface stress was removed using a JEOL* section polishing instrument at

*JEOL is a trademark of Japan Electron Optics Ltd., Tokyo.

Table I. Chemical Compositions of the Experimental Steel (Weight Percent)

C	Mn	P	S	Cr	Ni	O	N	Fe
0.14	30	< 0.004	< 0.008	7	0.26	< 0.001	< 0.005	bal.

8 kV for 10 minutes. The processing and analysis of the acquired images were performed using orientation imaging microscopy analysis software. The grain size was determined by the intercept method,[13] and each sample counted 300 to 500 grains. The TEM samples were ground down to ~ 30 μm with different sandpapers and subsequently electrochemically polished by the twin-jet method at a voltage of 23 V and a temperature of − 20 °C in a 10 pct perchlorate ethanol solution. The microstructure of all samples was observed along the longitudinal section containing the RD and the normal direction.

III. RESULTS AND DISCUSSION

A. *Microstructure Evolution*

Figure 1 presents the microstructure of the cold-rolled and subsequently annealed sample at 600 °C for 1 hour. Figure 1(a) shows the recrystallized structure with a volume fraction of ~ 85 pct and an average grain size of ~ 0.74 ± 0.35 μm. A small amount of deformation twin boundaries (DTBs) with a volume fraction of ~ 1.6 pct and an average lamellar spacing of ~ 43.4 ±30 nm were observed. Moreover, the low-angle grain boundaries (LAGBs) had a volume fraction of ~ 13.4 pct with an average lamellar spacing of ~ 69 ± 27 nm, while the volume fraction of recrystallization was very high. The size of the recrystallized grains and the spacing of the LAGBs and DTBs of the sample annealed at 600 °C for 1 hour were obtained by the calculation method proposed by Wang *et al.*,[35] where 2 is taken as the coefficient to convert the lamellar thickness into grain size. It was indicated that the mean grain size was ~ 0.65 ± 0.30 μm.

Figure 2 shows the microstructure and grain size distribution of the cold-rolled and subsequently annealed samples at 700 °C, 800 °C, and 900 °C for 1 hour. Figure 2(a) is the inverse pole figure (IPF) of the sample annealed at 700 °C. The deformation structure was replaced by equiaxed grains with random texture. Figure 2(b) presents the IPF of the sample annealed at 800 °C, where an insignificant growth of grains was observed. However, when the annealing temperature was increased to 900 °C, the grain size increased significantly (Figure 2(c)). The grain size of the completely recrystallized structure was measured by EBSD. Since the annealed twin boundaries can hinder the movement and sliding of dislocations as common grain boundaries, the statistics with regard to the grain size include the twin boundaries. The average grain sizes of the samples annealed at 700 °C, 800 °C, and 900 °C were 0.80 ± 0.58, 1.07 ± 0.57, and 5.75 ± 3.87 μm, respectively. With increasing annealing temperature, the grain size gradually increased. In the later tests, it

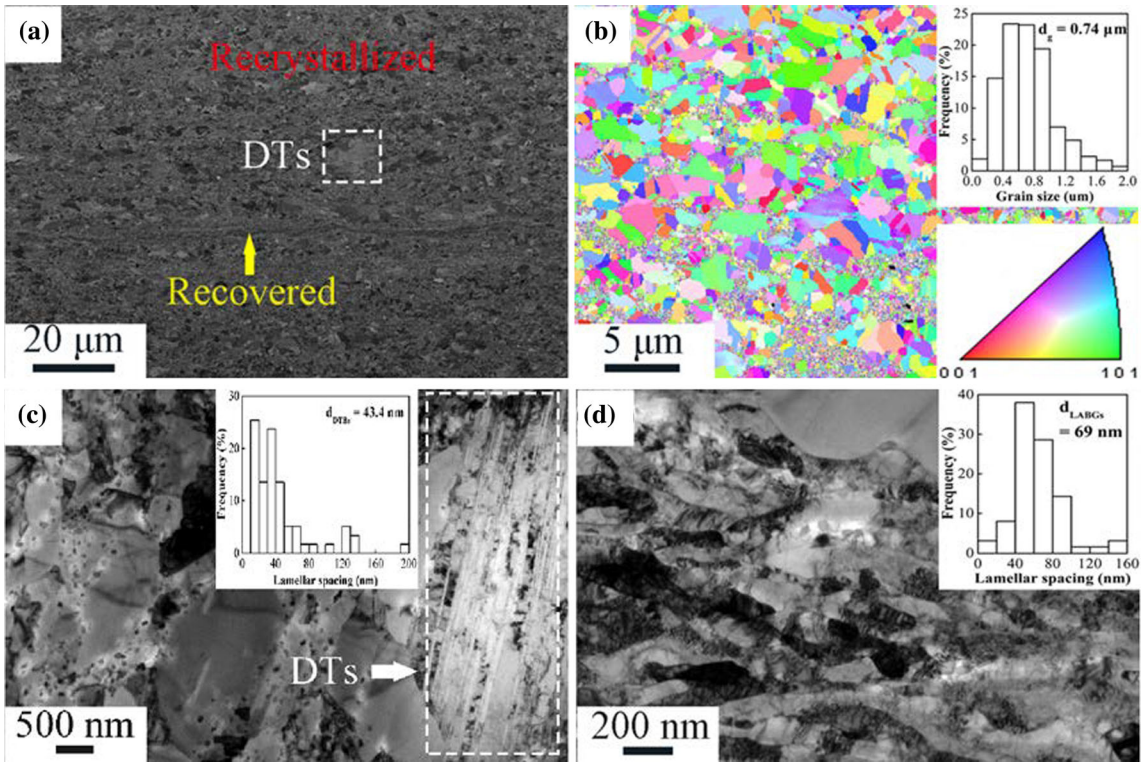

Fig. 1—Microstructure of the sample cold rolled to 95 pct, followed by subsequent annealing at 600 °C for 1 h: (*a*) ECCI, (*b*) recrystallized IPF, and (*c*) and (*d*) TEM image.

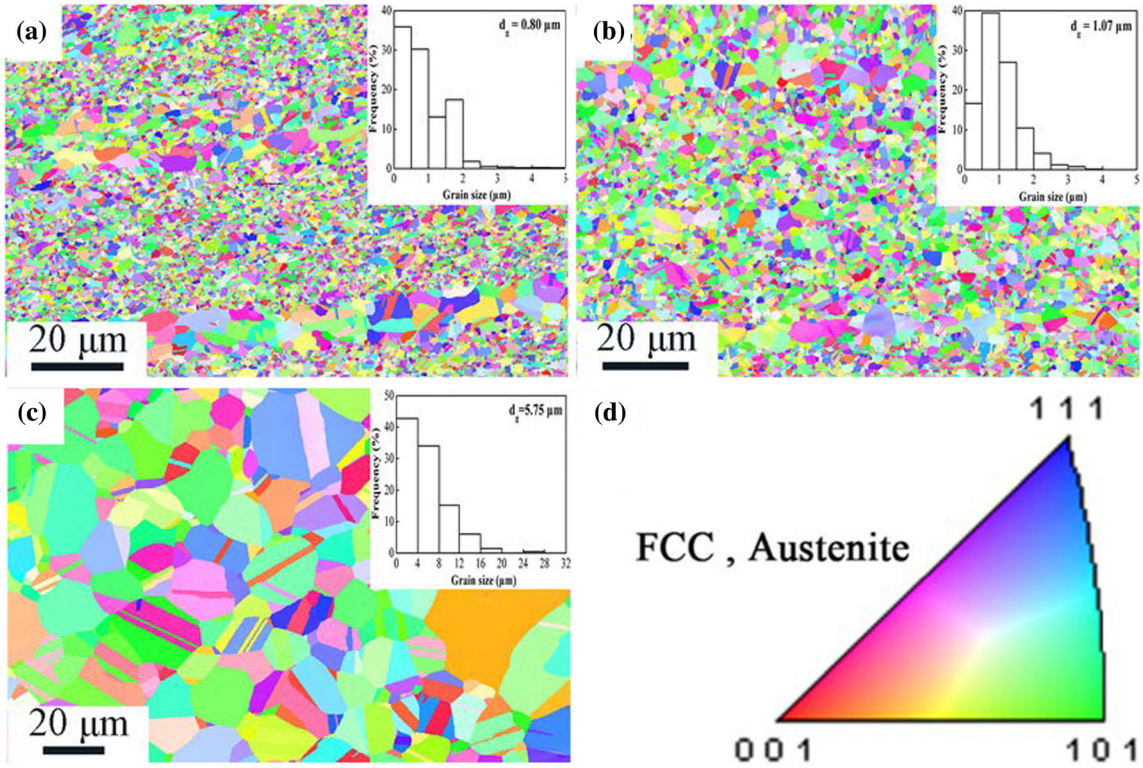

Fig. 2—IPF images and the distribution of grain sizes in the samples cold rolled to 95 pct and annealed for 1 h at different temperatures. (*a*) IPF image of the sample cold rolled to 95 pct and annealed for 1 h at 700 °C, (*b*) IPF image of the sample cold rolled to 95 pct and annealed for 1 h at 800 °C, and (*c*) IPF image of the sample cold rolled to 95 pct and annealed for 1 h at 900 °C. (*d*) The color scheme for orientation of grains in inverse pole figure maps.

was demonstrated that the dislocation density decreased with increasing annealing temperature, providing space for the generation and accumulation of more dislocations during the tensile deformation process.[36]

B. *Carbide Precipitation*

Figure 3 demonstrates the TEM images of the microstructure and size distribution of the precipitated carbides in the samples annealed in the temperature range of 600 °C to 900 °C for 1 hour. In the sample annealed at 600 °C, recrystallized grains and fine precipitation of carbide particles were observed. In addition, Figure 3(a) exhibits some nonrecrystallized regions. When the annealing temperature was increased to 700 °C, completely recrystallized grains and an increased amount of carbide particles were observed (Figure 3(b)). Maruyama *et al.*[37] proposed that a smaller size and larger number of particles can induce a significant strengthening effect on the material. Moreover, Roussel *et al.*[38] reported that carbides can effectively hinder the movement of dislocations, thus improving the yield strength of the material. Figures 3(a) through (c) show that the carbides were distributed in the grain interior, while only a few carbide particles were distributed in the grain boundaries. The inset in Figure 3(b) shows the diffraction pattern of the carbide, which indicates that the carbide was $Cr_{23}C_6$. The crystal structure of $Cr_{23}C_6$ is face-centered-cubic (fcc), which is related to the lattice of an adjacent austenite grain in accord with the cube-cube orientation relationship.[39] The generation of $Cr_{23}C_6$ can reduce the content of C, Cr, and other austenite stabilizing elements in austenite and significantly reduce the stability of austenite. Thus, $Cr_{23}C_6$ can promote deformation-induced martensite transformation during the deformation process.[40] However, according to the results of our previous study,[34] in both the fine- and coarse-grained samples, no martensite was produced after tensile fracture.

At the same time, a small number of carbide particles are distributed in dislocations, which are favorable for the precipitation of $Cr_{23}C_6$. When the annealing temperature was increased to 900 °C, no carbides were produced due to the increase in the solubility of the alloy elements and C in the austenite matrix, and the structure was composed of equiaxed recrystallized grains with a small number of annealing twins (Figure 3(d)). With the increase of the annealing temperature, these noncoherent $Cr_{23}C_6$ and austenite interfaces with high interfacial energy were conducive to migration, resulting in the growth of $Cr_{23}C_6$.[41] The average carbide sizes in the samples annealed at 600 °C, 700 °C, and 800 °C for 1 hour were approximately 39 ± 18.6, 53 ± 21.8, and 69 ± 18.6 nm, respectively. In Figures 3(a) through (c), stacking faults were observed. Table II presents the microstructure, lamellar spacing, grain size, and carbide size of the investigated steel cold rolled to a reduction of

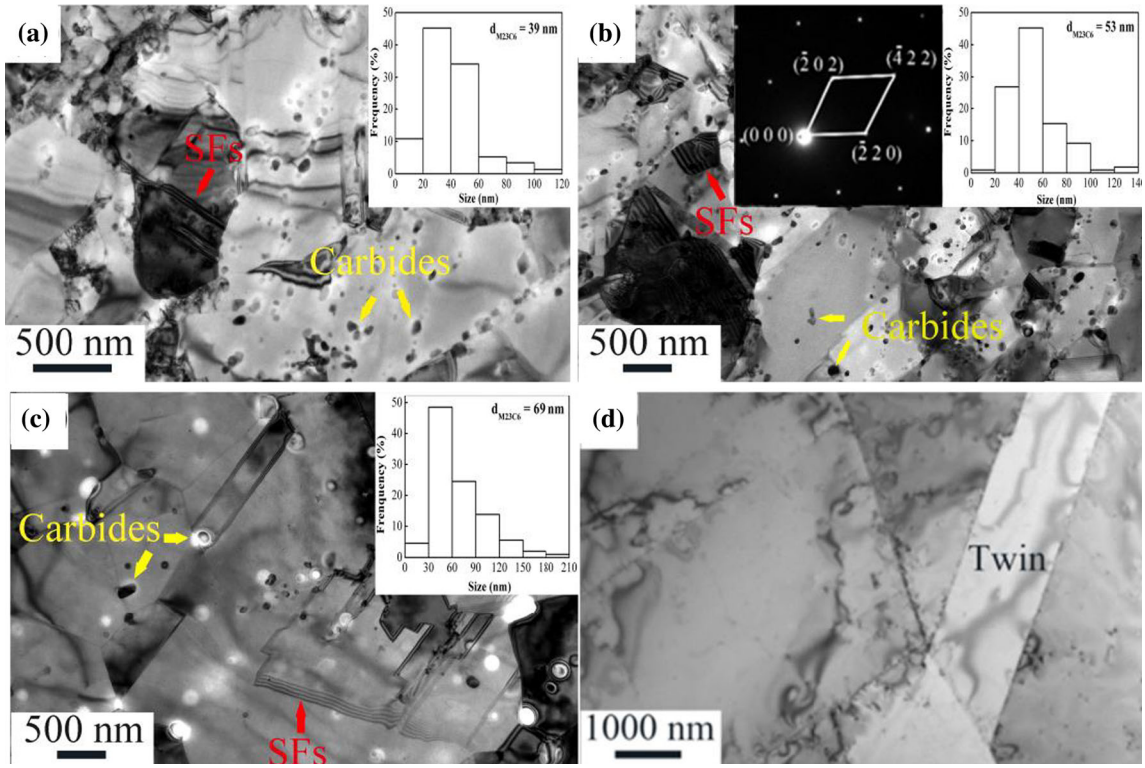

Fig. 3—TEM images and the distribution of carbide sizes in the samples of cold rolled to 95 pct and flowed by annealed for 1 h at different temperatures: (*a*) 600 °C, (*b*) 700 °C, (*c*) 800 °C, and (*d*) 900 °C.

Table II. Microstructure and Structural Parameters Determined for the Investigated Steel Cold Rolled to 95 Pct Followed by Annealing Under Different Conditions

Sample	Annealing Temperature (°C)	Microstructure	Lamellar Spacing (nm)/Grain Size (μm)	Carbide Size (nm)	Grain Size (μm)
1	600	composite structure: lamellar (13.4 pct)	69 ± 27	39 ± 18.6	0.65 ± 0.30
		deformation twins (1.6 pct)	43.4 ± 30		
		recrystallized (85 pct)	0.74 ± 0.35		
2	700	equiaxed grains	0.80 ± 0.58	53 ± 21.8	0.80 ± 0.58
3	800	equiaxed grains	1.07 ± 0.57	69 ± 33.8	1.07 ± 0.57
4	900	equiaxed grains	5.75 ± 3.87	—	5.75 ± 3.87

95 pct followed by annealing at different temperatures. The carbide particles stimulate more nuclei and hinder the growth of grains.[26,36] Consequently, the recrystallization level and grain size of the experimental steel after cold rolling to 95 pct reduction followed by annealing were much smaller than those of other high-manganese steels without particles annealed at similar temperatures.[42,43]

C. *Tensile Properties*

Figure 4 shows the engineering stress-strain (Figure 4(a)) and work hardening (Figure 4(b)) curves of different samples, according to which the yield and tensile strength decreased and the uniform and total elongation increased with increasing annealing temperature. After annealing at 700 °C, ultrafine grains with an average size of 0.8 μm and nanoscale carbides were generated, the yield strength reached 679 MPa, and the uniform and total elongations were 25.6 and 38.4 pct, respectively. Based on Figure 4(b), the strain hardening rate can be divided into three stages after annealing at 600 °C, 700 °C, and 800 °C. Compared to that of the samples annealed at 700 °C and 800 °C, the decreasing trend of the third stage of the work hardening rate at 600 °C is more apparent, indicating that fracture occurred earlier. While the strain hardening rate of the samples annealed at 900 °C exhibited a decreasing trend, it was maintained at a higher level for a longer time, which is consistent with the experimental results with the highest elongation. The $M_{23}C_6$ carbides in the experimental steel and the deformation twins generated

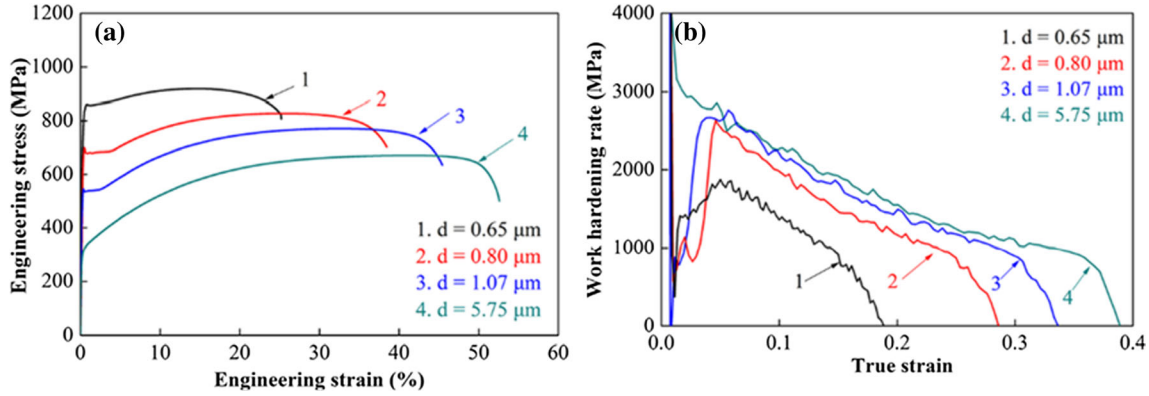

Fig. 4—(*a*) Engineering stress-strain curves of samples with different grain sizes and (*b*) the work hardening rate.

during the tensile process hinder the movement of dislocations, resulting in dislocation accumulation and an increase in the work hardening rate. However, during the tensile process of the samples annealed at 900 °C, a large number of deformation twins were produced (introduced in Section D). Therefore, the highest work hardening rate was maintained even without the presence of carbides in the austenite matrix.

D. *Stacking-Fault Energy and Deformation Mechanism*

In general, the stacking faults in the austenite phase determine the tensile deformation behavior of austenitic high-manganese steels. The stacking-fault energy of samples with different grain size can be calculated based on a modified equation of a thermodynamic model that takes the effect of grain size into consideration:[18,44–49]

$$\Gamma = 2\rho(\Delta G^{\gamma\to\varepsilon} + \Delta G_{ex}) + 2\sigma^{\gamma\to\varepsilon} \quad [1]$$

where Γ is the stacking-fault energy, ρ is the molar planar density along planes, $\Delta G^{\gamma\to\varepsilon}$ is the free energy for $\gamma \to \varepsilon$ phase transformation, ΔG_{ex} is the excess free energy due to the grain boundaries, and $\sigma^{\gamma\to\varepsilon}$ is the γ/ε interfacial energy, which can be expressed as[50]

$$\begin{aligned}\Delta G^{\gamma\to\varepsilon} =& X_{Fe}\Delta G^{\gamma\to\varepsilon}_{Fe} + X_{Mn}\Delta G^{\gamma\to\varepsilon}_{Mn} + X_C\Delta G^{\gamma\to\varepsilon}_{C} \\ &+ X_{Cr}\Delta G^{\gamma\to\varepsilon}_{Cr} + X_{Ni}\Delta G^{\gamma\to\varepsilon}_{Ni} \\ &+ X_{Fe}X_{Mn}\Delta\Omega^{\gamma\to\varepsilon}_{FeMn} + X_{Fe}X_c\Delta\Omega^{\gamma\to\varepsilon}_{Fec} \\ &+ X_{Fe}X_{Cr}\Delta\Omega^{\gamma\to\varepsilon}_{FeCr} + X_{Fe}X_{Ni}\Delta\Omega^{\gamma\to\varepsilon}_{FeNi} \\ &+ X_{Mn}X_C\Delta\Omega^{\gamma\to x}_{MnC} + X_{Cr}X_{Ni}\Delta\Omega^{\gamma\to\varepsilon}_{CrNi} + \Delta G^{\gamma\to\varepsilon}_{mg}\end{aligned} \quad [2]$$

where X_i is the atomic molar fraction of the i element, $\Delta G_i^{\gamma\to\varepsilon}$ is the free energy for $\gamma \to \varepsilon$ phase transformation of the I element, $\Delta\Omega_{ij}^{\gamma\to\varepsilon}$ is the free energy of the interaction between i and j during the $\gamma \to \varepsilon$ phase transformation, and $\Delta G_{mg}^{\gamma\to\varepsilon}$ is the free energy contribution due to the magnetic transition, which can be expressed as

$$\Delta G_{ex} = 170.06\exp\left(\frac{-d}{18.55}\right) \quad [3]$$

where d is the grain size.

The values of the stacking-fault energy (calculated according to Eqs. [1] through [3]), yield strength, tensile strength, uniform elongation, and total elongation for samples with different grain size are given in Table III. Due to the low stacking-fault energy of high-manganese steel, stacking faults can be easily formed, as shown in Figure 3. The decrease of the stacking-fault energy leads to widening of the stacking-fault space; thus, cross-slips rarely occur, which is conducive to the generation of deformation twins.

In order to identify the tensile deformation mechanism of the annealed specimens, the evolution of the microstructure during tensile deformation was investigated. Lee *et al.*[18] reported that a medium stacking-fault energy ($20 \le \gamma \le 50$ mJ/m^2) favors deformation twinning instead of martensitic transformation. According to Table III, the stacking-fault energy of all samples with different grain size was within the range that can induce the production of deformation twins. Our previous study confirmed that deformation twins are produced in ultra-fine-grained experimental steel under tensile deformation.[34] Figure 5 shows the electron channeling contrast images (ECCIs) of the samples annealed in the temperature range of 600 °C to 900 °C after tensile deformation to fracture, which indicate that deformation twins existed in all samples and their amount increased with increasing annealing temperature. Figure 6 shows the dependence of the deformation twin volume fraction on strain. In the fine-grained samples, the percentage of deformation twins was not significantly increased after fracture compared to that at 10 pct strain (Figure 6). However, in the samples annealed at 900 °C, the proportion of deformation twins in the microstructure was significantly increased after fracture compared to that under different tensile strains. This indicates that the generation of deformation twins can be seriously inhibited by grain refinement.

Deformation twins play a very important role in obtaining TWIP steel with excellent work hardening properties,[51] since they can prevent dislocation sliding as the traditional grain boundaries,[9] subdivide the initial grains into independent grains, reduce the average free path of dislocation slip, and strongly enhance the

Table III. Grain Size, Stacking-Fault Energy, and Tensile Properties of the Investigated Steel

Grain Size (μm)	Stacking-Fault Energy (mJ/m^2)	Yield Strength (MPa)	Tensile Strength (MPa)	Total Elongation (Pct)
0.65 ± 0.30	37.6	857	918	25.2
0.80 ± 0.58	37.5	679	827	38.4
1.07 ± 0.57	37.3	535	770	45.4
5.75 ± 3.87	35.0	322	671	52.6

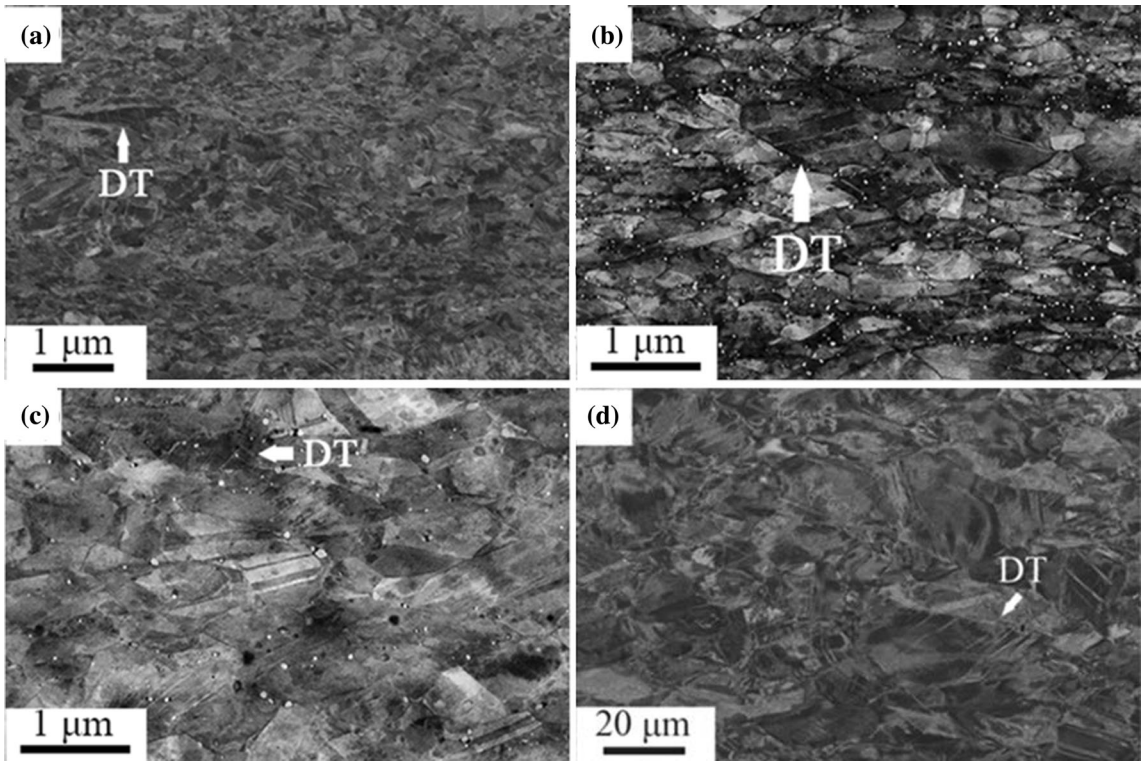

Fig. 5—ECCI images of samples with different grain sizes after tensile to fracture: (*a*) 0.65 μm, (*b*) 0.80 μm, (*c*) 1.07 μm, and (*d*) 5.75 μm.

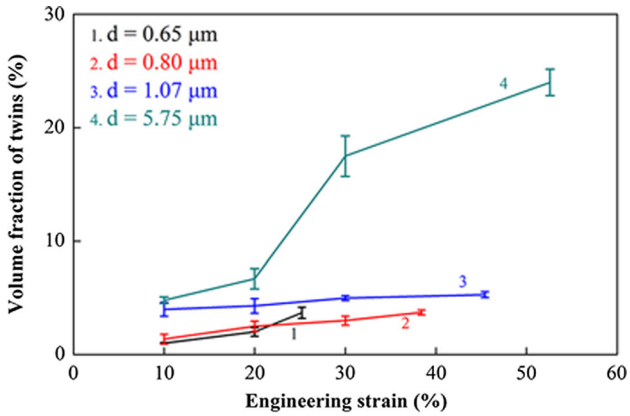

Fig. 6—Volume fraction of the deformation twins with different grain sizes at different tensile strains.

work hardening rate. The interaction between deformation twins and precipitated particles in austenitic high-manganese steel has been rarely reported. Chateau *et al.*[52] investigated Fe-22Mn-0.6C-0.21V and reported that the precipitated particles have no effect on the growth of deformation twins. Consequently, in this study, the interaction between deformation twins and precipitated particles needs to be further investigated.

The characteristics of Fe-30Mn and Fe-30Mn-0.5C (both in wt pct) were investigated by Wang *et al.*[53] Their results indicated that C can improve the yield strength with a higher work hardening rate before the generation of deformation twins during tensile deformation, and it is favorable for their formation. In addition, high-density deformation twins were found in Fe-30Mn-0.5C, which endow the material to maintain a high work hardening rate and elongation. These outcomes were induced by the interaction of C with

dislocations, as well as its effect on the stacking-fault energy.

E. *Strengthening Methods*

A decrease in grain size will increase the grain boundary area, enhance the resistance to dislocation movement, and improve the yield strength of high-manganese steels. The Hall–Petch equation takes the effect of grain size into consideration[54]:

$$\sigma_g = \mathrm{k}d_g^{-\frac{1}{2}} \quad [4]$$

where d_g is the grain size and k is 6.5 MPa mm$^{1/2}$. The grain size and yield strength were experimentally obtained and calculated by the least-squares method. The mean grain sizes d_g after annealing at 600 °C, 700 °C, 800 °C, and 900 °C for 1 hour were 0.65, 0.80, 1.07, and 5.75 μm, respectively. Since the samples annealed at 900 °C experience no precipitation strengthening and dislocation strengthening, the Hall–Petch relationship of coarse-grained structures used in our previous study was employed to calculate the grain boundary strengthening.[34]

Precipitation strengthening is related to the precipitation particle size d_p and the precipitation volume fraction f. The precipitation strengthening stress σ_p can be determined by the Ashby–Orowan equation[55]:

$$\sigma_P = 9.549 \times 10^3 \frac{f^{\frac{1}{2}}}{d_p} \ln(20.417 d_p) \quad [5]$$

where d_p is the precipitation particle size and f is the precipitation volume fraction, which, in the samples annealed at 600 °C, 700 °C, and 800 °C, was 2.6, 3.5, and 4.5 pct, respectively.

Solution strengthening is one of the main strengthening methods for metal materials, which is mainly achieved by the uniform distribution of the constituent atoms. When Cr atoms dissolve in the matrix to form a solid solution, lattice distortion occurs in the matrix. The interaction between the stress field caused by lattice distortion and that around the dislocations makes dislocation movement more difficult. Consequently, the shear stress required for dislocation slip will increase to overcome this pinning effect.[55] The σ_s due to solid solution strengthening can be expressed as[56]

$$\sigma_s = G\varepsilon\left(\frac{X_f}{4}\right)^{\frac{1}{2}} \quad [6]$$

where X_f denotes the concentration of the solute atoms and ε denotes the fractional difference between the diameter of the parent atoms and that of the solute atoms. Taking into consideration the dissolution of solute Cr atoms into the Fe matrix of the alloy, the fractional difference between the diameter of the Cr atoms and the matrix alloy is 0.008 and G is the shear modulus of the alloy,[50] which can be expressed as[16]

$$G = G_{\mathrm{Fe}}X_{\mathrm{Fe}} + G_{\mathrm{Mn}}X_{\mathrm{Mn}} + G_{\mathrm{Cr}}X_{\mathrm{Cr}} + G_{\mathrm{Ni}}X_{\mathrm{Ni}} \quad [7]$$

where X is the atomic fraction. The shear moduli of pure Fe, Mn, Cr, and Ni are 82, 79.5, 115, and 76 GPa,[57] respectively. While the effect of carbon on G was neglected, it was considered in the atomic fraction.[16] The shear modulus of the alloy was 83 GPa.

When the steel was annealed at 600 °C, 700 °C, and 800 °C, the fractions of the produced precipitates were 2.6, 3.5, and 4.5 pct, in which Cr accounted for 2.2, 3.3, and 4.2 pct, respectively. Therefore, the values of X_f were 5.2, 4.6, and 3.1 pct, respectively. After annealing at 900 °C, no carbides were produced and the value of X_f was 7.42 pct.

Dislocation strengthening is also one of the most effective strengthening methods for metal materials. When the dislocation density in a metal is high, the dislocation movement can easily trigger an interaction between dislocations and generate dislocation jogs and tangles, resulting in obstacles to dislocation movement. Consequently, plastic deformation cannot continue, thus improving the strength of the steel. It can be determined according to the following equation[58]:

$$\sigma_d = M\alpha \mathbf{b} G\rho^{\frac{1}{2}} \quad [8]$$

where M is the average Taylor factor, which is 3.06 for austenitic steels; α is a geometrical factor, which has been determined to be 0.35 for fcc structure[59]; $\boldsymbol{b}$ is the magnitude of the Burgers vector, which is equal to 0.25 nm; G is the shear modulus, which is 83 GPa for the investigated steel; and ρ is the dislocation density, which can be determined according to the following equation[60]:

$$\rho = 2\sqrt{3}(e^2)^{\frac{1}{2}}/d \times b \quad [9]$$

where $(e^2)^{\frac{1}{2}}$ is the average lattice strain,d is the size of the coherent diffraction area, and $\mathbf{b}$ is the magnitude of the Burgers vector. Based on Figure 7, the dislocation densities of 600 °C, 700 °C, and 800 °C were 1.45 × 10^{14}, 3.73 × 10^{13}, and 2.36 × 10^{13} m^{-2}, respectively. Since there were almost no dislocations in the sample annealed at 900 °C, the dislocation density was ignored.

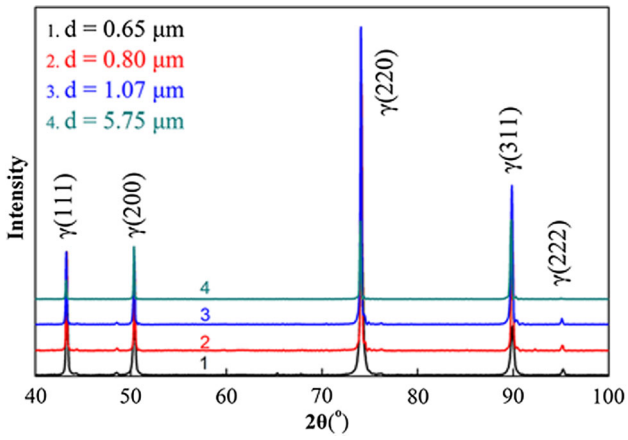

Fig. 7—XRD patterns of samples with different grain sizes.

Table IV. Strengthen Mechanisms on the Yield Stress

Grain Size (μm)	σ_g (MPa)	σ_p (MPa)	σ_s (MPa)	σ_p (MPa)	σ_0 (MPa)	Calculated Yield Strength (MPa)	Measured Yield Strength (MPa)
0.65 ± 0.30	255	264	76	267	22	884	857
0.80 ± 0.58	230	235	67	135	22	689	679
1.07 ± 0.57	199	212	58	107	22	598	535
5.75 ± 3.87	192	—	90	—	22	304	322

The lattice friction represents the resistance of the lattice to dislocation movement and can be determined according to the following equations[61]:

$$\sigma_0 = \sqrt{3}\tau_0 \quad [10]$$

$$\tau_0 = 2 \times 10^{-4} G \quad [11]$$

where σ_0 is the lattice friction, τ_0 is the shear stress for dislocation movement, and G is the shear modulus. The contribution of the different strengthening methods to yield strength is presented in Table IV.

In summary, fine-grain strengthening, precipitation strengthening, and dislocation strengthening have significant effects on the yield strength of the experimental steel, while the effects of solution strengthening and lattice friction are relatively weaker.

IV. CONCLUSIONS

Based on the results on microstructure evolution, carbide precipitation behavior, and tensile properties of Fe-30Mn-0.14C-7Cr-0.26Ni (in wt pct) high-manganese steel cold rolled and annealed at temperatures ranging between 500 °C and 900 °C for 1 hour, the following conclusions can be drawn.

1. Grain size increases with increasing annealing temperature. The stacking-fault energy decreases with increasing grain size. Above an annealing temperature of 600 °C, the carbides begin to precipitate, and the size of the carbide particles increases with increasing annealing temperature. Due to the presence of carbides, the grain growth at temperatures from 600 °C (0.65 μm) to 800 °C (1.07 μm) is not significant. When the annealing temperature is increased to 900 °C, no carbides are produced and the grain size increases significantly.
2. The carbides are identified as $Cr_{23}C_6$, which precipitate principally inside the recrystallized grains, while a small portion of the carbides precipitate in the dislocations, and only a few carbides precipitate in the grain boundaries.
3. A large amount of nanoscale carbides precipitate in the ultra-fine-grain structure after annealing at 700 °C for 1 hour, resulting in a good combination of yield strength (679 MPa) and ductility (total elongation of 38.4 pct). This is attributed to the combination of carbide precipitation, grain refinement, and presence of deformation twins.
4. Based on the statistics of the proportion of deformation twins in the microstructure annealed at 600 °C to 900 °C under different strains, it has been revealed that the generation of deformation twins can be seriously inhibited by grain refinement. The interaction between deformation twins and precipitated particles requires further investigation.
5. According to the calculation results, precipitation strengthening, grain boundary strengthening, and dislocation strengthening have significant effects on the yield strength of samples annealed at 600 °C, 700 °C, and 800 °C for 1 hour.

ACKNOWLEDGMENTS

The authors gratefully acknowledge the support from the National Nature Science Foundation of China (Grant Nos. 51871194 and 52001274) and the National Natural Foundation of Hebei Province, China (Grant No. E2018203312). One of the authors (YZ) acknowledges the support from the European Research Council (ERC) under the European Union's Horizon 2020 research and innovation programme (Grant Agreement No 788567, M4D).

DATA AVAILABILITY

The data sets generated for this study are available upon request from the corresponding author.

CONFLICT OF INTEREST

On behalf of all authors, the corresponding author states that there is no conflict of interest.

REFERENCES

1. O. Grässel, L. Krüger, G. Frommeyer, and L.W. Meyer: *Int. J. Plast.*, 2000, vol. 16, pp. 1391–1409.
2. C. Haase, S.G. Chowdhury, L.A. Barrales-Mora, D.A. Molodov, and G. Gottstein: *Metall. Mater. Trans. A*, 2012, vol. 43A, pp. 911–22.
3. O. Bouaziz, S. Allain, C.P. Scott, P. Cugy, and D. Barbier: *Curr. Opin. Solid State Mater. Sci.*, 2011, vol. 15, pp. 141–68.
4. Y. Lü, D.A. Molodov, and G. Gottstein: *Acta Mater.*, 2011, vol. 59, pp. 3229–43.

5. M. Koyama, Y. Shimomura, A. Chiba, E. Akiyama, and K. Tsuzaki: *Scripta Mater*., 2017, vol. 141, pp. 20–23.
6. J. Hufenbach, F. Kochta, H. Wendrock, A. Voss, L. Giebeler, S. Oswald, S. Pilz, U. Kühn, A. Lode, M. Gelinsky, and A. Gebert: *Mater. Des*., 2018, vol. 142, pp. 22–35.
7. L. Bracke, K. Verbeken, L. Kestens, and J. Penning: *Acta Mater*., 2009, vol. 57, pp. 1512–24.
8. H. Li, F. Yin, T. Sawaguchi, K. Ogawa, X. Zhao, and K. Tsuzaki: *Mater. Sci. Eng. A*, 2008, vol. 49, pp. 4217–26.
9. V. Shterner, I.B. Timokhina, and H. Beladi: *Mater. Sci. Eng. A*, 2016, vol. 669, pp. 437–46.
10. I. Gutierrez-Urrutia and D. Raabe: *Acta Mater*., 2012, vol. 60, pp. 5791–5802.
11. K. Renard and P.J. Jacques: *Mater. Sci. Eng. A*, 2012, vol. 542, pp. 8–14.
12. H.Z. Wang, P. Yang, W.M. Mao, and F.Y. Lu: *J. Alloys Compds*., 2013, vol. 558, pp. 26–33.
13. J.B. Seol, J.E. Jung, Y.W. Jang, and C.G. Park: *Acta Mater*., 2013, vol. 61, pp. 558–78.
14. V. Shterner, I.B. Timokhina, and H. Beladi: *Adv. Mater. Res*., 2014, vol. 922, pp. 676–81.
15. S. Allain, J.P. Chateau, and O. Bouaziz: *Mater. Sci. Eng. A*, 2004, vols. 387–389, pp. 143–47.
16. K.-T. Park, K.G. Jin, S.H. Han, S.W. Hwang, K. Choil, and C.S. Lee: *Mater. Sci. Eng. A*, 2010, vol. 527, pp. 3651–61.
17. S. Allain, O. Bouaziz, and J.P. Chateau: *Scripta Mater*., 2010, vol. 62, pp. 500–03.
18. S.I. Lee, S.Y. Lee, J. Han, and B. Hwang: *Mater. Sci. Eng. A*, 2019, vol. 742, pp. 334–43.
19. K.M. Rahman, V.A. Vorontsov, and D. Dye: *Acta Mater*., 2015, vol. 89, pp. 247–57.
20. M. Koyama, T. Sawaguchi, and K. Tsuzaki: *Mater. Sci. Eng. A*, 2011, vol. 530, pp. 659–63.
21. I. Gutierrez-Urrutia, S. Zaefferer, and D. Raabe: *Mater. Sci. Eng. A*, 2010, vol. 527, pp. 3552–60.
22. S. Kang, J.G. Jung, M. Kang, W. Woo, and Y.K. Lee: *Mater. Sci. Eng. A*, 2016, vol. 652, pp. 212–20.
23. B.C. De Cooman, Y. Estrin, and S.K. Kim: *Acta Mater*., 2018, vol. 142, pp. 283–362.
24. T. Yang, Y.L. Zhao, Y. Tong, Z.B. Jiao, J. Wei, J.X. Cai, X.D. Han, D. Chen, A. Hu, J.J. Kai, K. Lu, Y. Liu, and C.T. Liu: *Science*, 2018, vol. 362, pp. 933–37.
25. K. Zhang, H.Y. Wen, B.B. Zhao, X.P. Dong, and L.T. Zhang: *Mater. Charact*., 2019, vol. 155, p. 109792.
26. C. Scott, B. Remy, J.-L. Collet, A. Cael, C. Bao, F. Danoix, B. Malard, and C. Curfs: *Int. J. Mater. Res*., 2011, vol. 102, pp. 538–49.
27. H. Kubo, K. Nakamura, S. Farjami, and T. Maruyama: *Mater. Sci. Eng. A*, 2004, vol. 378, pp. 343–48.
28. Y. Yazawa, T. Furuhara, and T. Maki: *Acta Mater*., 2004, vol. 52, pp. 3727–36.
29. K.H. Han: *Mater. Sci. Eng. A*, 2000, vol. 279, pp. 1–9.
30. S. Kajiwara, D.Z. Liu, T. Kikuchi, and N. Shinya: *Scripta Mater*., 2001, vol. 44, pp. 2809–14.
31. J. Moon, H.-Y. Ha, S.-J. Park, T.-H. Lee, J.H. Jang, C.-H. Lee, H.N. Han, and H.-U. Hong: *J. Alloys Compds*., 2019, vol. 775, pp. 1136–46.
32. Y.S. Zhang, X.M. Zhu, and S.H. Zhong: *Corr. Sci*., 2004, vol. 46, pp. 853–76.
33. S.S.M. Tavares, M.L. Laurya, H.N. Farneze, R.V. Landim, J.A.C. Velasco, and J.L.M. Andia: *Eng. Fail. Anal*., 2019, vol. 104, pp. 331–40.
34. X.M. Chen, Y.H. Wang, J.C. Xiong, G.Y. Li, Y.Z. Tian, W.Q. Cao, and T.S. Wang: *Front. Mater*., 2020, vol. 7.
35. Y.H. Wang, J.M. Kang, Y. Peng, T.S. Wang, N. Hansen, and X.X. Huang: *Scripta Mater*., 2018, vol. 155, pp. 41–45.
36. S. Deb, S.K. Panigrahi, and M. Weiss: *Mater. Charact*., 2019, vol. 154, pp. 80–93.
37. K. Maruyama, K. Sawada, and J.-I. Koike: *ISIJ Int*., 2001, vol. 41, pp. 641–53.
38. M. Roussel, X. Saurage, M. Perez, D. Magné, A. Hauet, A. Steckrneyer, M. Vermont, T. Chaise, and M. Couvrat: *Materials*, 2018, vol. 4, pp. 331–39.
39. S.H. Byun, N. Kang, T.H. Lee, S.K. Ahn, H.W. Lee, W.S. Chang, and K.M. Cho: *Metall. Mater. Int*., 2012, vol. 18, pp. 201–07.
40. Y.M. He, Y.H. Wang, K. Guo, and T.S. Wang: *Mater. Sci. Eng. A*, 2017, vol. 708, pp. 248–53.
41. K. Kaneko, T. Fukunaga, K. Yamada, N. Nakada, M. Kikuchi, Z. Saghi, J.S. Barnard, and P.A. Midgley: *Scripta Mater*., 2011, vol. 65, pp. 509–12.
42. Y.H. Wang, B.D. Shi, Y.M. He, H.W. Zhang, Y. Peng, and T.S. Wang: *Materials*, 2018, vol. 11, pp. 253–61.
43. Y.H. Wang, J.M. Kang, Y. Peng, T.S. Wang, N. Hansen, and X.X. Huang: *J. Mater. Sci. Technol*., 2018, vol. 34, pp. 229–33.
44. S. Curtze, V.T. Kuokkala, A. Oikari, J. Tälonen, and H. Hänninen: *Acta Mater*., 2011, vol. 59, pp. 1068–76.
45. S. Allain, J.P. Chateau, O. Bouaziz, S. Migot, and N. Guelton: *Mater. Sci. Eng. A*, 2004, vol. 387, pp. 158–62.
46. O. Bouaziz and N. Guelton: *Mater. Sci. Eng. A*, 2001, vols. 319–321, pp. 246–49.
47. P.J. Brofman and G.S. Ansell: *Metall. Mater. Trans. A*, 1978, vol. 9A, pp. 879–80.
48. W.S. Yang and C.M. Wan: *J. Mater. Sci*., 1990, vol. 25, pp. 1821–23.
49. L. Lin, T.Y. Hsu, and Y. Zu: *Calphad*, 1997, vol. 21, pp. 443–48.
50. A.S. Hamada, L.P. Karjalainen, and M.C. Somani: *Mater. Sci. Eng. A*, 2007, vol. 467, pp. 114–24.
51. P. Kusakin, A. Belyakov, C. Haase, R. Kaibyshev, and D.A. Molodov: *Mater. Sci. Eng. A*, 2014, vol. 617, pp. 52–60.
52. J.P. Chateau, A. Dumay, S. Allain, and A.J. Jacques: *JPCS*, 2010, vol. 240, p. 012023.
53. X. Wang, H.S. Zurob, J.D. Embury, X. Ren, and I. Yakubtsov: *Mater. Sci. Eng. A*, 2010, vol. 527, pp. 3785–91.
54. H. Wu, S. Huang, C.Y. Zhu, H.G. Zhu, and Z.H. Xie: *Prog. Nat. Sci. Mater*., 2020, vol. 30, pp. 239–45.
55. X.J. Wang, X.J. Sun, C. Song, H. Chen, W. Han, and F. Pana: *Mater. Sci. Eng. A*, 2017, vol. 698, pp. 110–16.
56. X.Z. Zhang, T.J. Chen, and Y.H. Qin: *Mater. Des*., 2016, vol. 99, pp. 182–92.
57. *Environmental Chemistry*, J.K. Barbalace Inc., 1995, https://environmentalchemistry.com/yogi/perioc, Accessed 22 Oct 1995.
58. H.H. Zhi, C. Zhang, S. Antonov, H.Y. Yu, T. Guo, and Y.J. Su: *Acta Mater*., 2020, vol. 195, pp. 371–82.
59. M. Sauzay and L.P. Kubin: *Progr. Mater. Sci*., 2011, vol. 56, pp. 725–84.
60. N. Gao and T.N. Baker: *ISIJ*, 1988, vol. 38, pp. 144–51.
61. P. Kusakin, A. Belyakov, D.A. Molodov, and R. Kaibyshev: *Mater. Sci. Eng. A*, 2017, vol. 687, pp. 82–84.